Bull. Mater. Sci. (2024) 47:170
https://doi.org/10.1007/s12034-024-03257-6

Effect of 10 MeV electron irradiation on hydroxyapatite (HAP)

ATHIRA K V RAJ[1,*], RUMU H BANERJEE[1] and P SENGUPTA[1,2]
[1]Materials Science Division, Bhabha Atomic Research Centre, Mumbai 400 085, India
[2]Homi Bhabha National Institute, Anushakti Nagar, Mumbai 400 085, India
*Author for correspondence (athirakvr@barc.gov.in)

MS received 10 January 2024; accepted 31 March 2024

Abstract. To understand the impact of radiation doses, polycrystalline hydroxyapatite (HAP) samples were exposed to 10 MeV electron irradiation, reaching doses of up to 20 MGy and their structural–thermal–optical properties were compared with unirradiated sample by using powder X–ray diffraction (XRD), energy-dispersive X–ray fluorescence (EDXRF), Fourier transform infrared spectroscopy (FTIR), scanning electron microscopy (SEM), thermogravimetric analysis (TGA) and photoluminescence (PL) measurements. The results suggest that the samples exhibit high-phase stability, though irradiation induces the formation of surface defects and oxygen vacancies, while leaving morphology unchanged. It was noted that the lattice contracts, leading to reduced bond lengths and an increase in bond covalency, consequently resulting in a decrease in charge transfer (CT) energy. This nephelauxetic (covalency) effect is associated with a red shift observed in the excitation spectrum. Additionally, a noticeable enhancement of luminescence intensity was exhibited by HAP-1MGy sample attribute to the structured alignment of defects and oxygen vacancies within the lattice. These findings imply the exceptional radiation durability of HAP even after exposure to high electron-irradiation doses.

Keywords. Hydroxyapatite (HAP); electron beam irradiation; defect luminescence.

1. Introduction

Nuclear power is the clean power source after hydroelectricity, which has expanded over the last decades, owing to its growing importance in meeting the global energy demands [1]. As per the latest report from the International Atomic Energy Agency (IAEA), there are ∼416 operational nuclear power reactors worldwide, with a combined net electrical capacity of 374.26 GW(e) [2]. However, one of the major challenges associated with energy generation from nuclear reactor operations is the management of radioactive waste (RW). This waste originates from diverse sources, including mining and fuel processing activities, spent fuel assemblies, ion exchange resins as well as from facilities like radioisotope production laboratories, radiopharmaceuticals for biomedical applications and other processes, such as membrane operation, evaporation and filtration [3–7]. Effectively handling this radioactive waste has been a global priority for numerous years. Presently, vitrification of HLW in the borosilicate glass matrix is the adapted technology [8]. However, there is a continuous exploration for developing newer ceramic waste forms to capture and immobilize radioactive substances offering an efficient and effective solution to environmental challenges.

To address this, extensive research has been conducted on crystalline ceramic waste forms to gain insights into radiation-induced behaviours, with the goal of immobilizing and incorporation of radionuclides [9–12]. Significant computational and experimental studies on apatite structure have provided valuable insights for designing chemically durable apatite/phosphate-based waste matrices. Apatite is an earth-abundant mineral bearing the chemical formula of $A_{10}(BO_4)_6X_2$ (A = Ca, Pb, rare earth, fission product elements or actinides; B = P, V, Si or Cr; X = OH, O or halogens). These matrices show potential for immobilizing salt waste streams, nuclear fission by-products, actinide elements and other radioactive isotopes. The apatite matrices can act as potential crystalline ceramic waste forms for high level nuclear waste owing to their crystal chemistry, structure flexibility, promising thermal stability and low leaching rate [13]. Hydroxyapatite (HAP: $Ca_{10}(PO_4)_6(OH)_2$), renders it, as a promising crystalline ceramic waste due to its thermal stability, structural adaptability and low leaching rate; and ease to plant scale synthesis (co-precipitation, sonochemical and hydrothermal techniques). Studies have revealed HAP's flexibility in its crystal structure, enabling the incorporation and retention of diverse cationic and anionic species, and creating vacancies within its framework [14].

Further, evaluating the influence of radiation on material stability remains as a most critical concern in developing matrices for nuclear waste immobilization or transmutation.

This article is part of the Special issue on 'Materials for energy and sustainable development'.

Published online: 23 July 2024

To assess radiation stability, various types of ionizing and nonionizing radiations, including swift heavy ions, alpha rays, X–rays, gamma rays and specific wavelengths of light are utilized [15,16]. Parthiban *et al* [17] investigated the effects of swift heavy ion irradiation on HAP using 100 MeV oxygen ions at three different fluences of 10^{12}, 10^{13} and 10^{14} ions cm^{-2}, confirming incomplete amorphization of HAP with an increase in fluence, accompanied by a reduction in particle size. Suljovrujic *et al* [18] studied the effects of gamma irradiation on structure and physicochemical properties of the HAP/poly-L-lactide (HAP/PLLA) composite. Some of the major results on various irradiation studies were listed in table 1. Previous studies on irradiation effects on HAP have revealed a myriad of impacts on various aspects including crystallinity, particle size, structural and mechanical properties, optical characteristics, formation of defect clusters, absorbability, and osteoconductivity. Among that, electron beam irradiation is highly significant in radiation stability studies due to its ability to facilitate controlled assessment of radiation effects and induce controlled defects in materials, mimicking radiation damage [19]. Further, the medium-lived β-emitter fission products, 137Cs and 90Sr constitute the largest fraction of the nuclear waste in terms of activity. These radionuclides have high solubility in water at all pH values and hence, can be found in the cooling water of the damaged power plants and its adjacent areas [20]. If HAP is chosen as a potential sorbent for these radionuclides or waste forms to confine these radionuclides, it is thus essential that the radiation stability of these matrices under β-emission or electron beam is studied. This is because in the present study, 10 MeV electron beam irradiation on HAP samples was conducted to simulate the effects of β-induced damage, as the nature of defects introduced into the system is expected to be similar in both cases. Among various radiation sources, electron beam irradiation from an electron accelerator stands out as one of the most prevalent and socially acceptable processes, given that accelerators offer fully controlled systems [21]. A few electron irradiation studies were reported on the HAP samples, in which they are more concentrated on the surface and physicochemical properties [22–26]. However, these are leading to an incomplete comprehension of its impact on the structure and induced levels of defects within the HAP lattice. Moreover, the creation of vacancy defects leads to changes in the electronic configuration of HAP, potentially resulting in luminescent properties. Pure or stoichiometric HAP typically lacks luminescence. Studies have indicated that defective or non-stoichiometric HAP displays pronounced inherent photoluminescence (PL) within the visible spectral range [27,28]. Utilizing this form of HAP, as a contrast agent without dopants, offers a non-toxic and environmentally friendly alternative.

To evaluate radiation stability and defect generation, our study examines the influence of electron-beam irradiation on HAP samples subjected to doses ranging from 1 to 20 MGy. Analysing the unirradiated and irradiated HAP samples involves characterizing their structure, morphology, electronic configuration and defects using various techniques: powder X–ray diffraction (XRD), energy-dispersive X–ray fluorescence (EDXRF), Fourier transform infrared spectroscopy (FTIR), scanning electron microscopy (SEM), thermogravimetric analysis (TGA)- and PL measurements.

2. Experimental

2.1 *Sample preparation*

Phase-pure HAP compositions conforming to the general formula $Ca_{10}(PO_4)_6(OH)_2$, were procured from Ceramat Private Limited. These HAP powders were synthesized via an aqueous precipitation method, a widely favoured technique for producing HAP powders without the use of organic solvents at a cost-effective rate [29]. The synthesis involved thorough mixing of calcium hydroxide ($Ca(OH)_2$) and orthophosphoric acid (H_3PO_4) in specified proportions, followed by calcination to achieve the desired powder. This reaction solely yielded water as the end product and involved no introduction of foreign elements. The adjusted ratio of phosphoric acid to calcium hydroxide was maintained to sustain a Ca^{2+} to P^{5+} ratio of 1.7.

2.2 *Irradiation of samples*

Electron irradiation of the specimens was carried out at the indigenously developed radiofrequency (RF) 10 MeV electron linear accelerator facility housed at Electron Beam

Table 1. List of various irradiation studies on $Ca_{10}(PO_4)_6(OH)_2$.

	Radiation	Dose/flux	Major findings	Reference
$Ca_{10}(PO_4)_6(OH)_2$	Kr^{2+} ions	1 MeV	Amorphization	[22]
$Ca_{10}(PO_4)_6(OH)_2$:Mg	Electron	2 and 50 Gy	Morphological and physiochemical modifications	[23]
$Ca_{10}(PO_4)_6(OH)_2$	Electron	460 kGy	Surface modification	[24]
$Ca_{10}(PO_4)_6(OH)_2$	High energy laser	21–500 J cm^{-2}	Structural transformation	[25]
Ca-hydroxyapatite	Gamma	200 kGy	Biomedical competency	[26]

Centre (EBC), Kharghar, Mumbai, India. Samples were irradiated at two doses, 1 and 20 MGy. Parameters used during electron irradiation of the specimens are listed in table 2. The electron accelerator operated at 1 kW beam power, 35 mA beam current and 2857 MHz RF. The detailed description of the system developed, is provided in Banerjee *et al* [19]. The specimen powder was filled in a nickel crucible; the sample depth was kept less than the penetration depth (usually < 2 cm). The irradiation treatments were carried out at room temperature (25 ± 2°C, RH 60%) under normal light conditions.

2.3 *Characterization techniques*

HAP samples were analysed using a Rigaku Miniflex 600 equipped with Ni-filtered CuKα radiation to obtain their powder XRD patterns. The measurements were conducted over a 2θ scan range of 10–80° with a step size of 0.01° s^{-1}. EDXRF of the HAP samples were done in Xenemetrix model: Genius IF EDXRF instrument. The measurements were conducted at a voltage of 30 kW, a current of 1000 μA and a measurement time of 100 s, utilizing a Ti secondary target. FTIR spectra of the samples were acquired employing a Bruker FTIR spectrometer INVENIO instrument in ambient air conditions. The spectrometer was equipped with a PIKE MIRacle attenuated total reflection (ATR) accessory featuring a ZnSe ATR crystal, a KBr beam splitter and a DLaTGS detector. The powder samples were mixed with KBr in the ratio of 1:150 and pressed to form a 13 mm diameter pellet. Spectra were collected with a resolution of 4 cm^{-1} across the spectral range of 400–4000 cm^{-1} in transmission mode, with 1-min collection times for both sample and background measurements. Data analysis was conducted using Bruker's Opus software. The sample morphology analysis was performed utilizing a Carl Zeiss EVO 18 SEM. Simultaneous TG-DTA measurements were conducted using a Netzsch thermo-balance (model no.: STA 409 PC Luxx system). Pt and Pt-10% Rh thermocouples served as the temperature and differential temperature sensors for all the experiments involving TG-DTA analysis. Re-crystallized alumina crucibles held the samples and reference materials. Precisely weighed samples were heated in either air or an inert atmosphere to the desired temperature at a heating rate of 10°C min^{-1}. High purity nitrogen acted as the purge gas. The TG-DTA data analysis was performed using the Proteus software from Netzsch. PL spectra of the samples were obtained utilizing the Edinburgh FL-920 spectrofluorimeter unit. This system incorporates a 450 W variable frequency (10–100 Hz) Xe-flash lamp designed for excitation purposes.

Table 2. Parameters used during electron irradiation of specimens.

Parameters	Values/condition
Accumulated dose	1, 20 MGy
Dose rate	1 MGy h^{-1}
Activation	Not observed
Mode of beam operation	Static holder, scanning electron beam
Beam power	1 kW

3. Results and discussion

3.1 *Calculation of range*

The maximum range, expressed as density thickness, is determined using the empirical formula established by Katz and Penfold [30]:

$$R_{\max}(\text{g cm}^{-2}) = 0.530 \times \text{E} - 0.106 \quad \text{for} \quad E > 2.5 \text{ MeV}, \tag{1}$$

where E = 10 MeV. The calculated $R_{\max}$ is found to be 5.194 g cm^{-2}. Accordingly, based on theoretical density value of HAP: 3.156 g cm^{-3}, electrons with an energy of 10 MeV will penetrate a depth of 1.65 cm within the HAP sample. Thickness of the aluminium foil used is 75 μm and the electron range within aluminium is determined to be 1.92 cm. Consequently, the electrons effectively traverse through the aluminium foil, rendering its absorption negligible. The fraction of Bremsstrahlung X–rays produced in HAP by a mono-energetic electron beam of 10 MeV is provided as follows:

$$f_{\text{e}} = 10^{-3} \times Z \times E. \tag{2}$$

Here, E represents the energy of electron or beta particle, which is 10 MeV in this case. Z is the average atomic number, determined from the atomic fractions of Ca, P, O, H, along with their respective atomic numbers: $Z_{\text{Ca}} = 20$, $Z_{\text{P}} = 15$, $Z_{\text{H}} = 1$ and $Z_{\text{O}} = 8$ and is given by $Z = 11.465$. Upon substitution of the given values, the fraction of X–rays generated by 10 MeV electron beam is 0.115.

In the present investigation, the electron displacement cross-section, σ_{d} was also calculated following the formula provided below [19]:

$$\sigma_{\text{d}} = 8\pi a^2 Z^2 E^2 / MC^2 E_{\text{d}}. \tag{3}$$

In this equation, a denotes the Bohr radius of a hydrogen atom (5.29 × 10–11 m), Z represents the atomic number and M signifies the mass of displaced atom. The variables E and E_{d} correspond to the energies involved, with E being 13.6 eV (Rydberg constant) and E_{d} denoting the threshold energies necessary to displace primary knock-on atoms (PKAs) from their lattice positions. The displacement cross-sections for calcium (Ca) and phosphorus (P) are calculated to be 36.4 and 49.87 b, respectively, as detailed in Banerjee *et al* [19].

3.2 *XRD*

Investigation of the crystalline structure of unirradiated and irradiated HAP samples were conducted using powder XRD analysis. All samples demonstrated a strong agreement with the documented diffraction pattern of $Ca_{10}(PO_4)_6(OH)_2$ (ICDD-PDF no: 9-0432; hexagonal; space group P63/m). No additional peaks attributable to impurities were detected, confirming the high crystallinity of the samples. The Rietveld refinement of all the samples was conducted utilizing the X'Pert high score plus program, with the detailed results given in figure 1. The starting models employed for the refinement process are listed in table 3. The obtained XRD pattern demonstrates a strong agreement between the refinement and space group across all aspects, reflected in goodness-of-fit values of 2.76, 2.65 and 2.59 for HAP, HAP-1MGy and HAP-20MGy, respectively. Comparison between the irradiated and unirradiated systems reveals a slight decrease in lattice size; HAP: $a = b = 9.4123$ Å, $c = 6.8842$ Å; HAP-1MGy: $a = b = 9.4056$ Å, $c = 6.8758$ Å and HAP-20MGy: $a = b = 9.4096$ Å, $c = 6.8816$ Å, accompanied by a corresponding lattice contraction in the irradiated samples. This shift is associated with the emergence of defects within HAP lattice following electron irradiation [31]. Molecular dynamics studies have established that the size of an oxygen vacancy is smaller than that of an oxygen ion [32]. Consequently, the introduction of more oxygen vacancies into the HAP lattice results in its contraction due to the smaller ionic size of the vacancies. This finding supports with previous research [31]. Specifically, a more pronounced lattice contraction is observed in the HAP subjected to a 1 MGy radiation dose compared to both the unirradiated HAP and 20 MGy HAP. This disparity can be attributed to the short-range ordering of generated oxygen vacancies within the HAP-1MGy lattice. However, as the irradiation doses increase, a greater number of oxygen vacancies are created, diminishing the ability to form short-range clusters. Correlation between defect clustering and the facilitated ordering of oxygen vacancies is supported by the enhanced PL emission intensity observed in the HAP-1MGy sample. The average crystallite size of the samples was determined using Scherer's equation. A decreasing trend was observed as the irradiation dose increased: $D_{HAP} = 113.8$ nm; $D_{HAP\text{-}1MGy} = 96.2$ nm; $D_{HAP\text{-}20MGy} = 92.3$ nm, respectively. Further, it was noted that there was a slight decrease in intensity and broadening of the Bragg peaks (figure 2), which is attributed to the decrease in crystallinity following irradiation.

3.3 *FTIR analysis*

The chemical structure of $Ca_{10}(PO_4)_6(OH)_2$ before and after electron irradiation is further analysed in detail via FTIR. Within HAP molecules, both phosphate and hydroxyl groups play essential roles in the infrared spectrum's vibrational range, as depicted in figure 3. These groups exhibit four fundamental vibrational modes: symmetric stretching, symmetric bending, asymmetric stretching and asymmetric bending, typical for phosphate tetrahedral [33]. Phosphate ions are expected to manifest four distinct vibrational modes denoted as v_1, v_2, v_3 and v_4. Among these, three stretching modes were clearly observed, occurring at approximate wavenumbers of 962, 1030 and 1088 cm^{-1}, while bending vibration peaks generated near to the wavenumbers 470, 565 and 600 cm^{-1}. The vibrations near 1088 and 1030 cm^{-1} are attributed to the asymmetric stretching vibration (v_3) of the PO_4 group, while the peak at 962 cm^{-1} is due to the symmetric stretching vibration (v_1). It is worth noting that a shoulder peak appearing around 870 cm^{-1} is likely related to the presence of carbonates in the sample [34]. Bending vibrations corresponding to the v_4 degenerate state were observed at wavenumbers of 565 and 600 cm^{-1}, while the v_2 bending vibration was noted at 470 cm^{-1}. The subsequent predominant FTIR-active group comprises the hydroxyl functional group, which is corroborated by the small peaks around 632 and 3565 cm^{-1}. These band positions align with previously reported findings, reinforcing the presence of hydroxyl groups within the structure [24]. The distinct phosphate peaks in the FTIR spectrum remained unchanged, indicating high structural stability of the HAP samples and there were no evident additional peaks corresponding to phosphate condensation observed within the spectra. The inset figure provides expanded view of the vibrational mode near 1075 cm^{-1}, revealing change in intensity in the stretching vibration of PO_4 group. The irradiated samples exhibited notably higher intensity compared to the unirradiated ones. This change suggests potential rearrangements of atoms of PO_4 group within the HAP lattice, potentially due to the defect formation. These alterations influence the vibrational modes, resulting in the intensified peaks observed in the spectrum. Furthermore, the FTIR analysis provides invaluable understanding of the structural stability of HAP samples after electron irradiation, underscoring the significance of these vibrational modes in characterizing the material's properties.

3.4 *Morphological analysis*

Figure 4 exhibits SEM micrographs of both unirradiated HAP and irradiated HAP-1MGy and HAP-20MGy powder samples. The particles are seen with some amount of aggregation with a size range of 1–10 μm. No additional morphology changes were observed in the samples across varying radiation doses. The elemental composition was verified by energy-dispersive spectrometer (EDS) analysis attached with SEM (figure 5). These analyses confirmed the presence of all the expected elements in the samples.

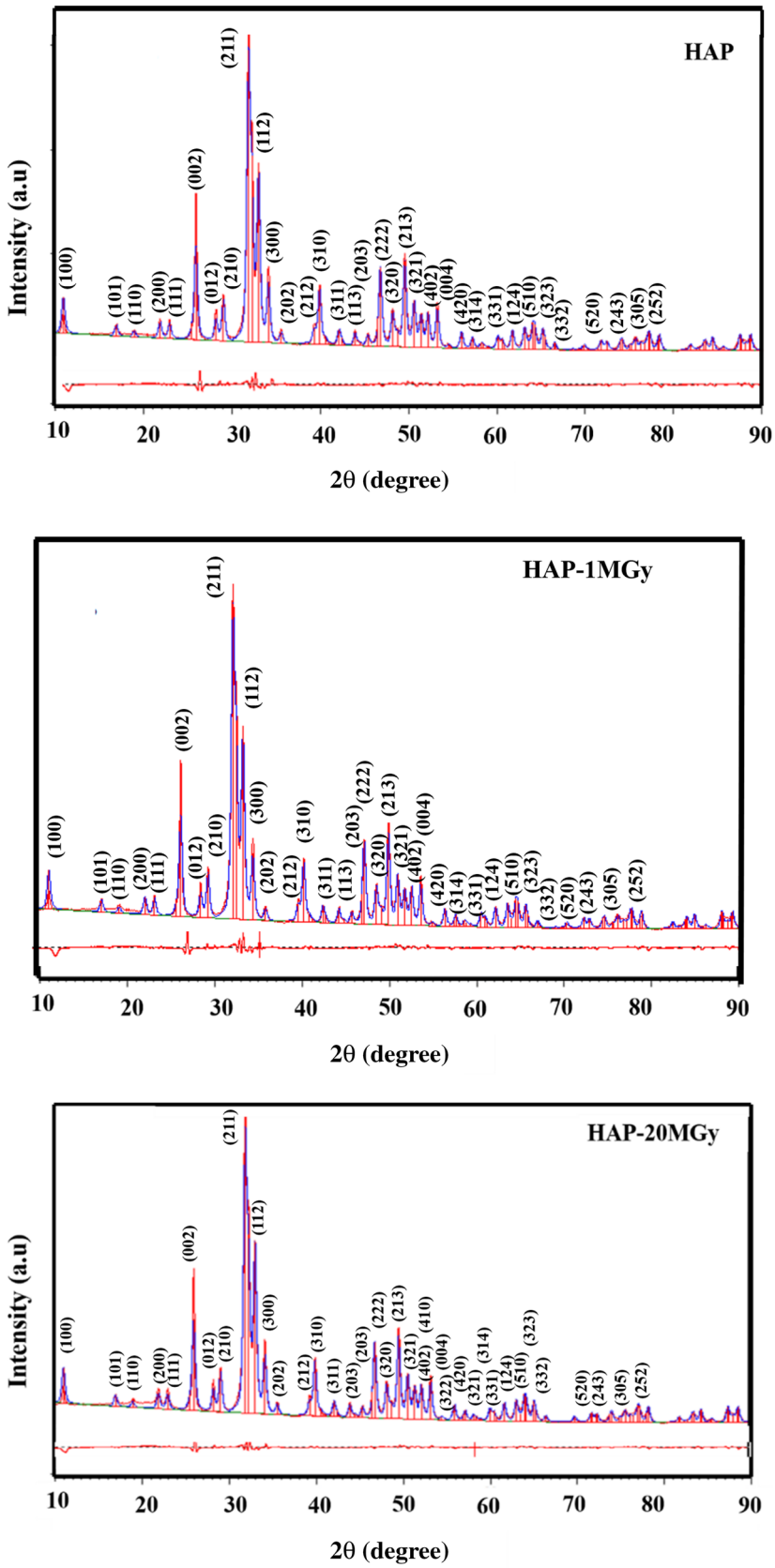

Figure 1. Observed (points), calculated (continuous line) and the difference in (bottom line) powder X–ray diffraction profiles of HAP, HAP-1MGy and HAP-20MGy samples obtained from the Rietveld refinement.

Table 3. Starting model of $Ca_{10}(PO_4)_6(OH)_2$.

Elements	Wyckoff positions	*x*	*y*	*z*	SOF
Ca	4f	0.3333	0.6667	0.0015	1
Ca	6h	0.2468	0.2534	0.2500	1
P	6h	0.3987	0.0302	0.2500	1
O	6h	0.1564	0.4848	0.2500	1
O	6h	0.5873	0.1222	0.2500	1
O	12i	0.3437	0.0858	0.0702	1
O	4e	0.0000	0.0000	0.1950	0.5
H	4e	0.0000	0.0000	0.608	0.5

3.5 *EDXRF analysis*

An assessment of the chemical elements in both unirradiated and irradiated HAP samples was conducted through EDXRF analysis. EDXRF analysis of HAP revealed discernible peaks for calcium (Ca) and phosphorus (P) exclusively, as the analysis could not include oxygen (O) and hydrogen (H) due to their lower atomic numbers. Further, this confirmed the phase purity of the samples, with detailed values presented in table 4. Additionally, the Ca^{2+}–P^{5+} ratio for the powdered samples was determined to be ~1.75, which is in close agreement with the Ca^{2+}–P^{5+} ratio of HAP reported in existing literature, i.e., 1.67 [35,36]. To gain further clarification on the increase in Ca/P ratio of the irradiation samples, EDS analyses were conducted, as illustrated in figure 5. Further, it was observed that the atomic weight percentage of oxygen decreases as irradiation doses increase, which is attributed to the emergence of oxygen vacancy defects within the lattice structure. The generation of defects was confirmed from the XRD analysis. HAP possesses a fixed stoichiometry

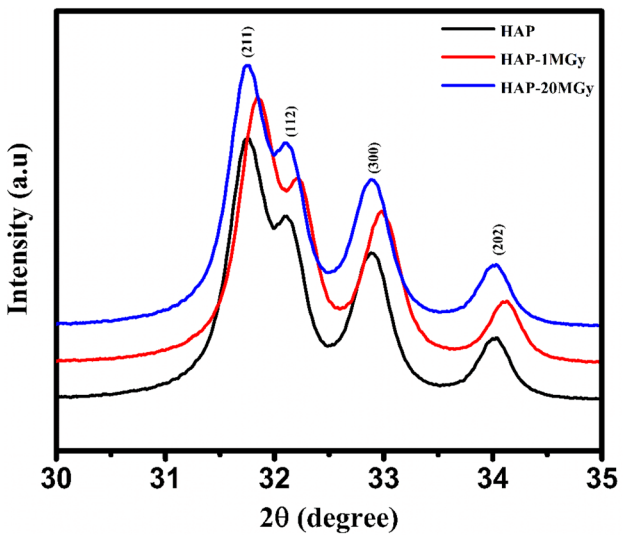

Figure 2. Powder XRD patterns of HAP, HAP-1MGy and HAP-20MGy within the 2θ range of 30–35°.

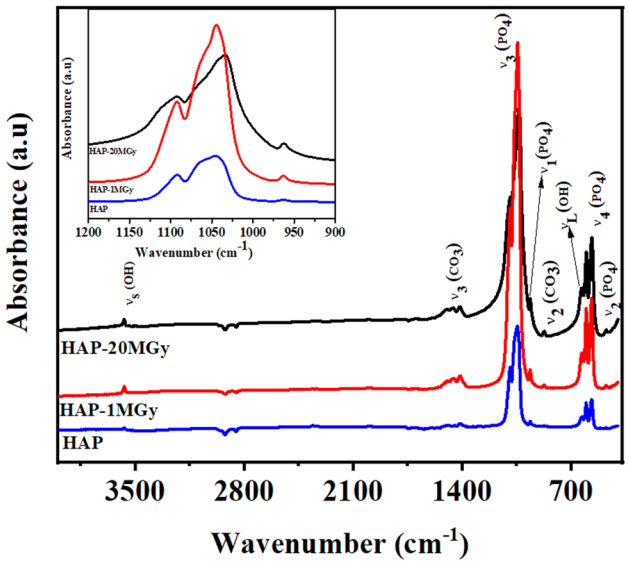

Figure 3. FTIR spectra of HAP, HAP-1MGy and HAP-20MGy samples and the inset figure provides the expanded view of the vibrational mode near wavenumber 1075 cm^{-1}.

involving calcium (Ca), phosphorus (P) and oxygen (O). Any disruption to this stoichiometry, such as the formation of oxygen vacancies, can introduce charge imbalances within the crystal lattice. To maintain charge neutrality, adjustments in the ratio of calcium to phosphorus atoms may occur. As a result of the generation of oxygen vacancy defects caused by irradiation, the Ca/P ratio was observed to increase in the irradiated samples.

3.6 *TGA*

Thermal stability of the unirradiated and irradiated HAP samples was examined through TGA in the temperature range of 50–1000°C. The findings clearly indicate a negligible weight loss within the investigated temperature range. Up to 700°C, HAP demonstrates remarkable thermal stability, evident from the uniformly progressing TG curve. However, at 800°C, a slight weight loss becomes apparent, which is evident from the TG analysis. The initial break in the curve correlates with a partial release of water and the dehydroxylation process within HAP. The subsequent break signifies the onset of thermal decomposition of HAP. The cumulative weight loss for the HAP, HAP-1MGy and HAP-20MGy samples were 2.46, 2.59 and 2.78%, respectively.

3.7 *PL analysis*

PL excitation spectrum of the HAP, HAP-1MGy and HAP-20MGy samples for an emission at 500 nm are depicted in figure 6. The spectrum includes a broad CT band ranging from 230 to 300 nm, attributed to the charge density

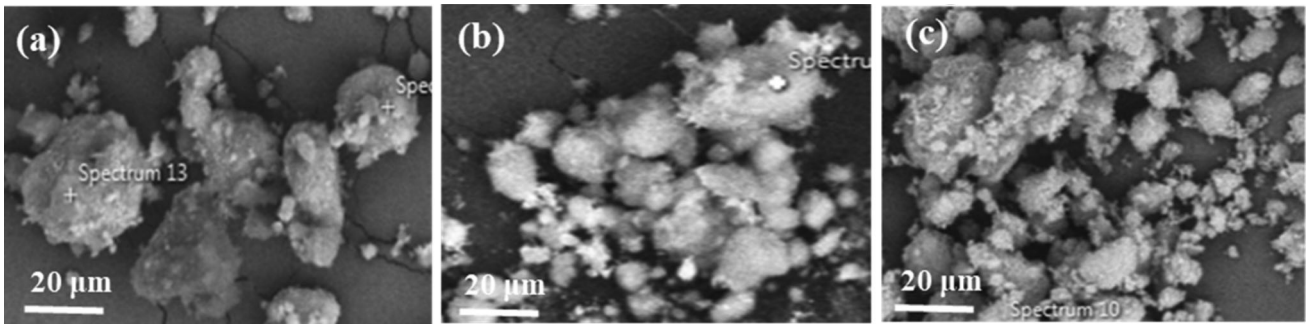

Figure 4. Typical SEM photographs of (**a**) HAP, (**b**) HAP-1MGy and (**c**) HAP-20MGy samples.

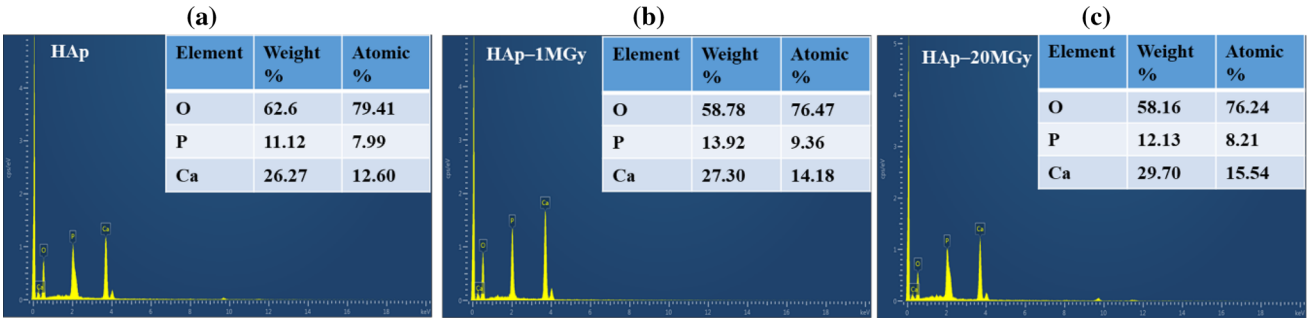

Figure 5. EDS spectra of (**a**) HAP, (**b**) HAP-1MGy and (**c**) HAP-20MGy samples.

Table 4. EDXRF results of HAP, HAP-1MGy and HAP-20MGy samples.

Compositions	X–ray emission energy, keV		Ca/P ratio
	Ca	P	
HAP	3.45	1.99	1.73 ± 0.01
HAP-1MGy	3.51	1.99	1.76 ± 0.02
HAP-20MGy	3.49	1.98	1.76 ± 0.01

redistribution from the 2p orbit of O^{2-} to the 3p orbit of P^{5+}. Upon increasing the electron irradiation dosage, a pronounced red shift in the CT band of HAP-1MGy sample is observed, while a slight red shift is observed in the HAP-20MGy sample. Additionally, a similar increasing trend in the intensity of CT band is evident with the rising irradiation dose. The emission spectra of HAP, HAP-1MGy and HAP-20MGy samples under 260 nm excitation, are shown in figure 7. Within the spectrum, intrinsic luminescence is evident, characterized by a violet emission at ∼425 nm and a sharp green emission around 500 nm. These emissions are attributed to CT transitions and distortions in PO_4 induced by defects or oxygen vacancies, respectively [37]. It was found that from the emission spectra, the electron irradiation significantly enhanced the luminescence attributed to defects or oxygen vacancies rather than the luminescence associated with CT transitions. Specifically, the HAP-1MGy sample exhibited the most pronounced emission

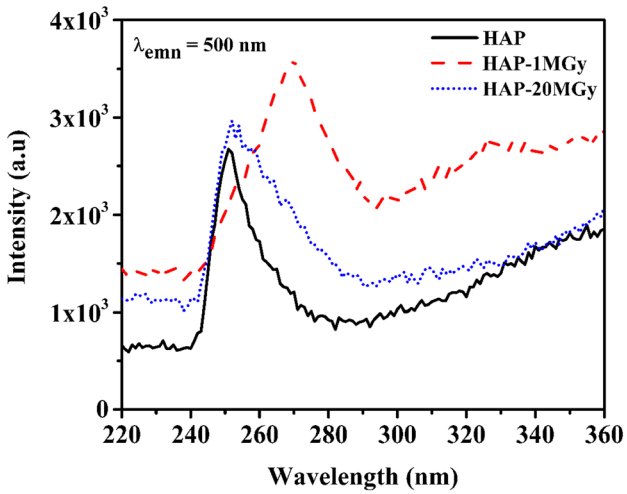

Figure 6. Photoluminescence excitation spectra of HAP, HAP-1MGy and HAP-20MGy samples for 500 nm emission.

intensity, exceeding that of both the HAP and HAP-20MGy samples.

A schematic representation outlining the intrinsic luminescence mechanism in HAP is shown in figure 8. Introduction of electron irradiation triggers the formation of defects, particularly oxygen vacancies within the HAP crystal lattice, consequently leading to luminescence emission within the system. Presence of these oxygen vacancies prompts for the generation of multiple holes close to the valence band (VB) edge [38]. Simultaneously, these vacancies induce the creation of shortened deep defects due

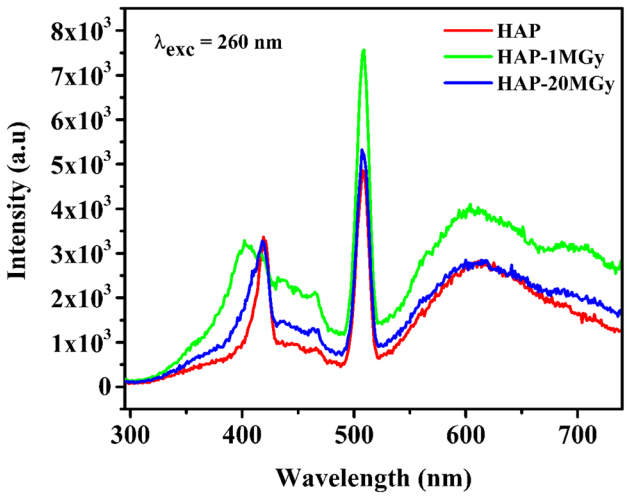

Figure 7. Photoluminescence emission spectra of HAP, HAP-1MGy and HAP-20MGy samples under 260 nm excitation.

to distortions occurring in phosphate tetrahedra within the band gap. This vacancy-induced phenomenon leads to an increased presence of holes, facilitating electron transitions from O 2*p* orbitals in the VB to P 3*p* orbitals in the CB through absorbed energy. The resultant photoemission process involves excited electrons returning to their ground state through radiation, as illustrated in figure 7.

3.8 *Discussion*

Electron irradiation prompts the creation of defects, such as oxygen vacancies, within the PO_4 tetrahedra. This concept becomes clearer when considering the displacement cross-section for phosphorous (P): 49.87 b and for calcium (Ca): 36.4 b due to energetic electrons. The incident electrons reveal a higher capability to displace P– ions within the lattice than the Ca–ions. These defects generated in the PO_4 tetrahedra act as energy level traps, serving as luminescent centres that generate emissions. As the electron irradiation doses increase, it was observed that the lattice contracts, resulting in a decrease in bond lengths and an increase in bond covalency. This enhanced covalency leads to a reduction in the CT energy. Consequently, this nephelauxetic (covalency) effect is associated with a red shift observed in the excitation spectrum [39]. Specifically, a more significant lattice contraction is evident in the 1 MGy radiation dose of HAP compared to both the unirradiated HAP and the 20 MGy HAP. Consequently, the pronounced nephelauxetic effect in the HAP-1MGy sample results in a more pronounced red shift in its CT band. The enhancement of luminescence in the HAP-1MGy sample is mainly attributed to combined effect of both nephelauxetic effect and the short range ordering of oxygen vacancies. Upon further increase in irradiation doses, an inverse covalency effect was observed, leading to a slight red shift in the CT band of HAP-20MGy sample. The enhancement of luminescence emission intensity is strongly dependent on the creation and arrangement of defects, notably oxygen vacancies. Electron irradiation played a significant role in enhancing these mechanisms by altering phosphate tetrahedra and generating oxygen-deficient tetrahedra (defects), consequently promoting a more organized alignment of oxygen vacancies within the lattice. However, as observed in the excitation spectra, owing to the inverse nephelauxetic effect, a larger number of disordered oxygen vacancies emerged and diffused within the lattice. These disorganized vacancies impose limitations on radiative transitions, consequently leading to the quenching of luminescence emission intensity at higher doses. In a nut shell, the inverse nephelauxetic effect along with disordered oxygen vacancies diminishes the luminescence intensity of HAP-20MGy sample. In the present study, it was discovered that HAP samples exhibit a defective, strong intrinsic PL across the visible spectrum, ranging from violet to green. This inherent property of HAP as a contrast agent, without the incorporation of dopants, represents a nontoxic, environmentally friendly alternative to activator-doped phosphors currently in use. Moreover, we substantiate the existence of vacancy defects through PL measurements.

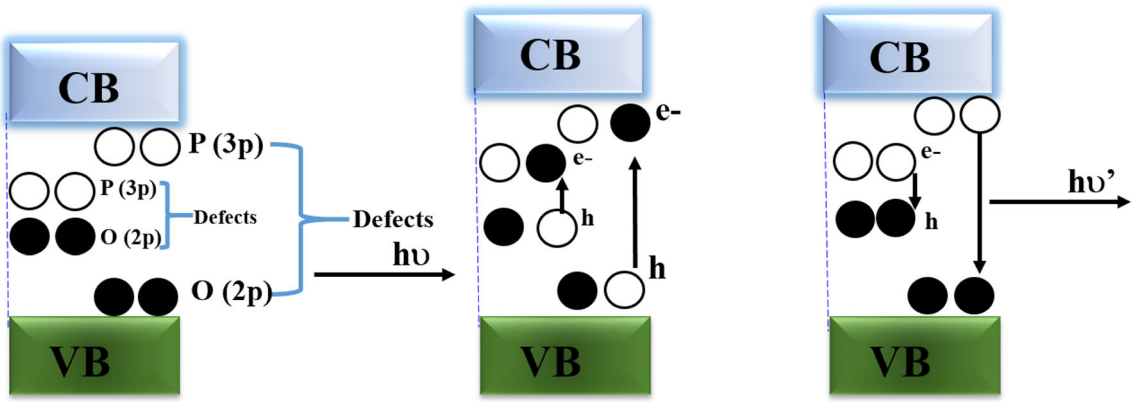

Figure 8. Schematic representation of the intrinsic defect luminescence mechanism of HAP.

Furthermore, the extensive analysis conducted on both unirradiated and electron-irradiated HAP samples provides crucial insights, such as the characteristic XRD peaks were retained in the irradiated samples, indicating substantial structural stability following electron irradiation. Additionally, irradiation induces the formation of surface defects and oxygen vacancies, while leaving the chemical composition and morphology unchanged. Moreover, PL studies strongly suggest the ordered configuration of oxygen vacancies within the HAP-1MGy sample. These findings imply the exceptional radiation durability of HAP even after exposure to high electron irradiation doses, highlighting its potential for serving as a viable host for immobilizing radioactive waste and as a phosphor material.

4. Conclusions

To investigate the effects of radiation doses, HAP samples were exposed to 10 MeV electron irradiation, reaching doses of up to 20 MGy. Notably, the HAP specimens showed no post-irradiation radioactivity. A comprehensive analysis employing powder XRD, EDXRF, FTIR, SEM, TGA and PL measurements, was conducted to evaluate the impact of electron beam irradiation on both unirradiated and irradiated HAP samples. The results indicated high structural stability within the samples, accompanied by irradiation-induced surface defect and oxygen vacancy formation, without altering the chemical composition or morphology. Notably, observed lattice contraction led to reduced bond lengths and increased bond covalency, resulting in a lowered CT energy and a corresponding red shift in the excitation spectrum. Additionally, the HAP-1MGy sample exhibited significantly enhanced luminescence intensity, attributed to the organized alignment of defects and oxygen vacancies within the lattice. These findings underscore the exceptional radiation durability of HAP, even after exposure to high electron irradiation doses, highlighting its potential for immobilizing radioactive waste and its applicability as a phosphor material.

Acknowledgements

The present study is funded by Department of Atomic Energy, Government of India project 'Irradiation induced transformations in nuclear materials' (Grant No.: R&D-058-2019). We thank Shri R B Chavan and Dr Nishant Chaudhary, Electron Beam Centre, BARC, for assistance in beam irradiation experiments. We are thankful to Dr Bhaskar Paul for SEM investigations and Dr V Sudarsan for providing the PL facility. We also thank Dr Archana Sharma, Director, Beam Technology Development Group and Dr R Tewari, Associate Director, Materials Group, Bhabha Atomic Research Centre, for their interests in the study and constant encouragement. We acknowledge the support of project trainee, Ms Ruchee Bhagwat, VIT, Vellore, in sample preparation and recording FTIR measurements.

References

[1] Sengupta P, Kaushik C P and Dey G K 2013 In: Ramkumar M (ed.) *On a sustainable future of the Earth's natural resources* (Berlin, Heidelberg: Springer Earth System Sciences, Springer)
[2] IAEA-PRIS-Power Reactor Information System, World statistics nuclear power capacity trend, Available: https://pris.iaea.org/pris/worldstatistics/worldtrendnuclearpowercapacity.aspx
[3] Iqbal S, Hassan M, Ryu H J and Yun J 2019 *RSC Adv.* **9** 34872
[4] Loon L R V and Hummel W 1999 *Nucl. Technol.* **128** 388
[5] IAEA-TECDOC-1051 1998 Management of radioactive waste from ^{99}Mo production
[6] Rahman R O A, Rakhimov R Z, Rakhimova N R and Ojovan M I (eds) 2015 *Cementitious materials for nuclear waste immobilization* (UK: Wiley & Sons)
[7] Pathak N, Das P, Chundawat B, Modak P and Modak B 2022 *J. Hazard. Mater.* **423** 126980
[8] Sengupta P, Dey K K, Halder R, Ajithkumar T G, Abraham G, Mishra R K *et al* 2015 *J. Am. Ceram. Soc.* **98** 88
[9] Zhou J, Yao T, Cao D, Lian J and Lu F 2018 *J. Nucl. Mater.* **512** 307
[10] Lu F Y, Shen Y Q, Sun X, Dong Z L, Ewing R C and Lian J 2013 *Acta Mater.* **61** 2984
[11] Zhou J R, Yao T K, Lian J, Shen Y Q, Dong Z L and Lu F Y 2016 *Nucl. Instrum. Methods Phys. Res. B: Beam Interact. Mater. Atoms* **379** 102
[12] Sickafus K E, Grimes R W, Valdez J A, Cleave A, Tang M, Ishimaru M *et al* 2007 *Nat. Mater.* **6** 217
[13] Jianren Z, Tiankai Y, Dongmei C, Jie L and Fengyuan L 2018 *J. Nucl. Mater.* **512** 307
[14] Carrera K, Huerta V, Orozco V, Matutes J, Fernandezd P, Graeve O A *et al* 2021 *Mater. Sci. Eng.* **271** 115308
[15] Banerjee R H, Swikisani M M N, Naina R, Harshala P, Nishant C, Mathi P *et al* 2024 *Ceram. Int.* **50** 2405
[16] Halder R, Pranesh S, Sudarsan V, Ghosh A, Bhukta A, Sharma G *et al* 2015 *J. Nucl. Mater.* **456** 359
[17] Parthiban S P, Suganthi R V, Girija E K, Elayaraja K, Kulriya P K, Katharria Y S *et al* 2008 *Nucl. Instrum. Methods Phys. Res.* **266** 911
[18] Suljovrujic E, Ignjatovic N and Uskokovic D 2003 *Radiat. Phys. Chem.* **67** 375
[19] Banerjee R H, Alexander R, Chaudhary N, Debnath A K, Sudarsan V, Sengupta P *et al* 2023 *Ceram. Int.* **49** 21324
[20] Banerjee R H, Nelwamondo S M M, Raje N, Parab H, Chaudhary N, Mathi P *et al* 2024 *Ceram. Int.* **50** 2405
[21] Chaudhary N, Singh A, Aswal D K, Debnath A K, Samanta S, Koiry S P *et al* 2017 *Synth. Met.* **231** 143
[22] Jianren Z, Mark K, Pete B and Fengyuan L 2021 *Materials* **18** 101154
[23] Bita B, Stancu E, Stroe D, Dumitrache M, Ciobanu S C, Iconaru S L *et al* 2022 *Polymers* **14** 582

[24] Guillaume B, Jean C H, Ulrich M, Phillipe S and Etienne B 2020 *Radiat. Phys. Chem.* **177** 109192
[25] Meurman J H, Hemmerlé J, Voegel J C, Rauhamaa M R and Luomanen M 1997 *Caries Res.* **31** 397
[26] Sahadat H, Aftab A S, Shirin A J, Monika M, Mashrafi B M, Saifur R *et al* 2023 *RSC Adv.* **13** 9654
[27] Verónica J H, Paloma F, Virginia G, Olivia A G and Manuel H 2020 *Appl. Mater. Today* **21** 100822
[28] Machado T R, Sczancoski J C, Beltrán-Mir H, Nogueira I C, Li M S, Andres J *et al* 2017 *J. Solid State Chem.* **249** 64
[29] Nayak A K 2010 *Int. J. Chemtech Res.* **2** 903
[30] Russell K C 1984 *Prog. Mater. Sci.* **28** 229
[31] Athira K V R, Rao P P, Sreena T S and Thara A T R 2017 *Phys. Chem. Chem. Phys.* **19** 20110
[32] Nakamura A 2010 *Solid State Ion.* **181** 1543
[33] Kourkoumelis N and Tzaphlidou M T 2010 *Sci. World J.* **10** 402
[34] Hossain M S and Ahmed S 2023 *RSC Adv.* **13** 14625
[35] Kay M I, Young R A and Posner A S 1964 *Nature* **204** 1050
[36] Singh G, Singh H and Sidhu B S 2014 *Bull. Mater. Sci.* **37** 1519
[37] Machado T R, Sczancoski J C, Mir H B, Li M S, Andres J, Cordoncillo E *et al* 2018 *Ceram. Int.* **44** 236
[38] Athira K V R, Rao P P, Sreena T S and Thara A T R 2018 *J. Mater. Sci.: Mater. Electron.* **29** 16647
[39] Linda T F, Rao P P, Mariyam T, Mahesh S K and Reshmi V R 2014 *J. Mater. Sci.: Mater. Electron.* **25** 2387